Earth System
Dynamics

Discussions

Minimal dynamical systems model of the northern hemisphere jet stream via embedding of climate data

Davide Faranda[1,2], Yuzuru Sato[3,2], Gabriele Messori[4, 1], Nicholas R. Moloney[5,2], and Pascal Yiou[1]

[1]Laboratoire des Sciences du Climat et de l'Environnement, UMR 8212 CEA-CNRS-UVSQ, Université Paris-Saclay, IPSL, 91191 Gif-sur-Yvette, France
[2]London Mathematical Laboratory, 8 Margravine Gardens London, W6 8RH, UK
[3]RIES / Department of Mathematics, Hokkaido University, Kita 20 Nichi 10, Kita-ku, Sapporo 001-0020, Japan
[4]Department of Meteorology and Bolin Centre for Climate Research, Stockholm University, 106 91, Stockholm, Sweden
[5]Department of Mathematics and Statistics, University of Reading, Reading RG6 6AX, UK

Correspondence: Davide Faranda (davide.faranda@lsce.ipsl.fr)

Abstract. We derive a minimal dynamical model for the northern hemisphere mid-latitude jet dynamics by embedding atmospheric data, and investigate its properties (bifurcation structure, stability, local dimensions) for different atmospheric flow regimes. We derive our model according to the following steps: i) obtain a 1-D description of the mid-latitude jet-stream by computing the position of the jet at each longitude using the ERA-Interim reanalysis, ii) use the embedding procedure to derive a map of the local jet position dynamics, iii) introduce the coupling and stochastic effects deriving from both atmospheric turbulence and topographic disturbances to the jet. We then analyze the dynamical properties of the model in different regimes: i) one that gives the closest representation of the properties extracted from real data, ii) one featuring a stronger jet (strong coupling), iii) one featuring a weaker jet (low coupling), iv) modified topography. We argue that such a simple model provides a useful description of the dynamical properties of the atmospheric jet.

10 *Copyright statement.* TEXT

1 Introduction

Jet streams are narrow, fast-flowing westerly air currents. They are a major feature of the large-scale atmospheric circulation and modulate the frequency, severity and persistence of weather events across the extra-tropics (e.g. Röthlisberger et al. (2016)). Their location and intensity also affects commercial aviation and shipping (Reiter and Nania, 1964; Hadlock and Kreitzberg,

15 1988; Williams and Joshi, 2013). Two types of atmospheric jets can be identified: thermally-driven subtropical jets, and eddy-driven jets associated with baroclinic instability at the polar front. In the Northern Hemisphere (NH), the two are not always clearly separated (Lee and Kim, 2003), and when considering monthly or longer time averages a single, spiral-shaped jet structure emerges (e.g. Archer and Caldeira, 2008). In this paper we consider a single NH jet (NHJ), rather than attempting to separate subtropical and eddy-driven jets (e.g. Belmecheri et al., 2017).

Even though the climatological NHJ is a westerly flow, it can present large meanders on a synoptic timescale (Koch et al., 2006; Röthlisberger et al., 2016). These can cause the local flow to become predominantly meridional, or can even determine a splitting of the jet (Haines and Malanotte-Rizzoli, 1991). The occurrence of these large meanders in the jet is often associated with extreme climate events such as temperature and precipitation extremes (e.g. Dole et al., 2011; Screen and Simmonds, 2014). Although jet dynamics are well understood in a climatological sense, our understanding of dynamical features such as jet breaking and meandering is still incomplete.

The dynamics of meanders and discontinuities in the jet has often been framed in terms of transitions between zonal and blocked flows. Legras and Ghil (1985) and Ghil (1987) used an intermediate complexity barotropic model with dissipation forcing and topography, and observed two distinct equilibria associated with the zonal and blocked flows. Similar mechanisms have been proposed by Mo and Ghil (1988) using experimental facilities (Weeks et al., 2000). However, there is no consensus about the nature of flow multistability, and a wide range of theoretical explanations and models have been proposed (e.g. Tung and Lindzen, 1979; Simmons et al., 1983; Frederiksen, 1982; Faranda et al., 2016b). Moreover, jet breaking has been described as a manifestation of multiple equilibria in asymmetrically forced flows (Hansen, 1986) or as a result of soliton–modon structures (McWilliams et al., 1981).

Here, the focus is not on the persistence and transitions between zonal and blocked regimes. Rather, we propose an alternative framework to diagnose the instantaneous meridional location of the jet from data and model this location using a simple stochastic coupled map lattice. We follow the approach outlined by Faranda et al. (2017c) to build a minimal model for the jet position by embedding atmospheric data obtained from the ERA-Interim dataset. This model is based on a coupled map lattice (CML). Each element of the lattice reflects the dynamics of the jet at each longitude. This CML is stochastically perturbed to account for baroclinic eddies and turbulence. The goal of the paper is to evaluate how this model represents the dynamical features of the jet.

The paper is organized as follows: we first give the details of the ERA-Interim data and of the jet detection algorithm (Section 2). We then present the stochastic coupled lattice map model and compute its bifurcation structure (Section 3). We then introduce some instantaneous dynamical indicators (Section 4) and use them to relate the conceptual model to state of the art global climate models and reanalysis data (Section 5). Finally, we highlight the open questions our results can answer and the new questions they pose (Section 6).

2 ERA-Interim data and jet position algorithm

The analysis is based on the ERA-Interim reanalysis of the European Centre for Medium Range Weather Forecasts Dee et al. (2011). We consider daily data with a 1° horizontal resolution over the period 1979–2016.

The jet position is diagnosed through a modified version of the approach of Woollings et al. (2010). We take daily mean wind-speed averaged over (200–400 hPa) and apply a 10-day low-pass Lanczos filter (Duchon, 1979). We then identify the latitudinal position of the jet at every longitude as the location of the strongest wind, over the band 15°–75° N. This approach

is intended to capture a "raw" measure of the jet variability. We then consider the longitude and time dependence of the latitude of the jet. This allows us to monitor the waviness of the jet.

We define an index of large jet meanders, or breaks, (Breaking Index, BRI) by the daily number of meridional variations in jet position of more than $10°$ of latitude across adjacent longitude gridpoints, except at longitude 0. The analysis presented in

5 this paper has been repeated for meridional variations between $5°$ and $15°$, with no significant qualitative differences.

A snapshot of the jet position, obtained for Feb 04th 1979, is shown in Figure 1, together with the time series of the daily jet position recorded in 1979 at longitude $120°$ W. An animation of the jet location for the year 1980 is provided in the supplementary video. Both the time series and the snapshot show jumps in the jet position, reflected in the BRI.

In order to embed the data and derive the effective maps of the dynamics, we remove the seasonal cycle from the data by

10 subtracting, longitude by longitude, the average meridional position for each calendar day and dividing by the standard deviation. For the deseasonalized data, the threshold for the computation of BRI corresponding to $10°$ latitude is 1.2.

3 Derivation of lattice jet model

We focus on the local dynamics divided into 360 cells, assuming that the dynamics in each cell is almost autonomous, but

15 perturbed by the external environment, i.e., the adjacent cells. The spatial continuity of the jet stream is modeled via the coupling of the local dynamics. The local dynamics are represented as a discrete map and the jet dynamics as a coupled map lattice (CML) Kaneko (1983). A diffusively coupled map is given by:

$$x_{n+1}^{(i)} = (1-\epsilon)f(x_n^{(i)}) + \frac{\epsilon}{2}\left[f(x_n^{(i-1)}) + f(x_n^{(i+1)})\right], \tag{1}$$

where $i = 1, 2, \ldots, N$, $\epsilon \in [0,1]$ and $x_n^{(i)} \in \mathbb{R}$. For the jet dynamics, we adopt the open flow model with uni-directional coupling

20 (Kaneko, 1985). We also include additive noise $\xi_n^{(i)}$, which perturbs the local dynamics $\{x_n^{(i)}\}$ at each cell acccording to:

$$x_{n+1}^{(i)} = (1-\epsilon)f(x_n^{(i)}) + \epsilon f(x_n^{(i-1)}) + \xi_n^{(i)}. \tag{2}$$

Here, we assume that the local dynamics are mostly affected by (upstream) coupling via the left-hand cell, with weak noisy perturbations. Periodic boundary conditions are applied with $N = 360$.

To extract the local dynamics, we construct an average return map. We first coarse-grain the state space into 500 partitions

25 with median $\bar{x}_n^{(i,k)}$, where $k \in \{1,\ldots,500\}$, and construct a return map $\tilde{f}$ via the first return plot of $(\bar{x}_n^{(i,k)}, \langle x_{n+1}^{(i,k)} \rangle)$ as follows:

$$\langle x^{(i,k)_{n+1}} \rangle = \tilde{f}(\bar{x}_n^{(i,k)}), \quad k \in \{1,\ldots,500\}. \tag{3}$$

From the observed data, the average return map $\tilde{f}(x)$ is approximated as

$$\tilde{f}(x) = \begin{cases} -\frac{A(A+x)}{A-c}, & x < -c, \\ \sinh(\beta x), & -c \le x \le c, \\ \frac{A(A-x)}{A-c}, & c < x, \end{cases} \tag{4}$$

where $\beta = 0.75$, $A = 3$, and $c = \sinh^{-1}(A)/\beta \approx 2.4246$, which is estimated from the extracted average return map. In the region where $|x| > c$, we have linear reflection effects. The functional forms of the return map are approximately the same at each longitude.

The noise ξ is a fundamental ingredient for the breaking of the jet and the transition between zonal and blocked states, as has also been shown through tank experiments and numerical simulations Jacoby et al. (2011). Indeed, in the absence of noise, the purely deterministic map results in a jet that settles on a central jet position (CJ) $x = 0$ at all longitudes. But with the addition of noise, jumps are observed between a northern jet position (NJ) $x \simeq +2$, a central jet position (CJ) $x = 0$, and a southern jet (SJ) position $x \simeq -2$. Physically, noise arises from sub-grid processes that affect the jet dynamics, such as convection or the interaction between the jet stream and gravity waves. These have been recognized as fundamental ingredients of jet breaking in both numerical simulations and experimental studies Williams et al. (2003, 2005). Translated to our model, these phenomena, ranging from a few meters to a few kilometers, implies a perturbation in the range $10^{-4} < \nu < 10^{-3}$, where ν is a random variable draw from a uniform distribution in $[-\delta, \delta]$. However, the model only exhibits jet breaking when $\delta \gtrsim 0.4$, which is too large to represent realistic corrections to the jet dynamics. We are therefore led to introduce further noise perturbations.

Another ingredient of the jet dynamics is the presence of topographic obstacles to the mid-latitude zonal flow. Mountain ranges and land-sea boundaries cause meridional deviations in the mean jet location (Tibaldi et al., 1980). This inhomogeneity can be modeled via a parameter r that mimics "spatial noise." Since the topography is at most a few kilometers in height, this translates to a perturbation of the order of 10^{-3} in the model. Reasonable geographical constraints are therefore: $r^{(i)} = 0.02$ ($i \in$ land) and $r^{(i)} = -0.04$ ($i \in$ ocean), where land spans the ranges $0 \le i < 161$ and $239 \le i < 301$, and ocean spans the ranges $161 \le i < 239$ and $301 \le i < 360$. Other parameter values are presented and tested in the next section.

A further important ingredient is the baroclinic activity associated with extra-tropical cyclones and anticyclones. These atmospheric features, on scales of order 10^{-3} km, can affect the jet position by several degrees of latitude. In our model, the effect of baroclinic waves is introduced through the block noise η^{bl}, where η takes the same value over bl blocks with an amplitude of order 1 (the one-dimensionalized size of cyclones/anticyclones). To determine a realistic length for bl, we reason as follows: if $N = 360$, each grid cell is about 100km wide. Assuming a typical scale of about 3000 km, the extra-tropical cyclones are therefore ≈ 30 blocks wide. However, the perturbations are associated with the cyclone radius rather than diameter: upstream of the cyclone, the jet will mostly be deviated southwards, while downstream of the cyclone, the jet will mostly be deviated northwards. We therefore take the block perturbation to be of size $15 < bl < 20$ blocks. In conclusion, the noise term in our model is comprised of

$$\xi_n^{(i)} = \nu_n^{(i)} + r^{(i)} + \eta_n^{(i)}, \tag{5}$$

where ν, r and η represent the effects of small turbulent disturbances, spatial inhomogeneities, and baroclinic eddies, respectively (see the schematic picture in Figure 2).

Owing to the uni-directional coupling in the model, the local dynamics $\{x_n^{(i)}\}$ at i can be approximated by the following non-autonomous (or random) dynamical system;

$$x_{n+1}^{(i)} = \tilde{f}(x_n^{(i)}) + r^{(i)} + p_n^{(i)}, \tag{6}$$

Earth System
Dynamics
Discussions

where $r^{(i)} \in \{-0.04, 0.02\}$, $p_n^{(i)} = \epsilon \Delta_n^{(i)} + \nu_n^{(i)} + \eta_n^{(i)}$, and $\Delta_n^{(i)} = \tilde{f}(x_n^{(i-1)}) - \tilde{f}(x_n^{(i)})$. The new variable $p_n^{(i)}$ represents the external perturbation from the adjacent environment. Assuming that the time averages $\langle \Delta_n^{(i)} \rangle$, $\langle \nu_n^{(i)} \rangle$, and $\langle \eta_n^{(i)} \rangle$ are all 0 by symmetry, then $\langle p_n^{(i)} \rangle \approx 0$, so that we recover the average return map at cell i given in Eq. (3).

In the absence of interactions, $|p_n^{(i)}| \to 0$, there are three invariant sets: a stable fixed point at $x \approx 0$, and two unstable chaotic sets at $x \approx \pm 2$. With a non-autonomous external force $p_n^{(i)}$, the resulting dynamics may exhibit escape behaviour from the fixed point to the chaotic regions with positive Lyapunov exponents. The external perturbation $p_n^{(i)}$ can be approximated by a random variable drawn from a uniform distribution in $[-\kappa, \kappa]$. The bifurcation diagrams as a function of κ over land ($r^{(i)} = -0.04$) and ocean ($r^{(i)} = 0.02$) are shown in Figure 4. They both indicate a bifurcation to chaotic and partially chaotic behaviour (Sato et al.). The different values of r over land and ocean give rise to an asymmetry in the minimal invariant sets, which delimit the accessible region of the dynamics with respect to all possible external perturbations. In Figure 4, these minimal invariant sets are in grey, while a realization of the dynamics with $\{p_n^{(i)}\}$ is given by the black dots. With $r^{(i)} = -0.04$ ($r^{(i)} = 0.02$) and $0.136 < \kappa < 0.217$ ($0.156 < \kappa < 0.196$), there is a small chance to reach SJ (NJ) positions and no chance to reach NJ (SJ) positions. This is reflected in the skewed x distribution for larger values of κ. In the interest of conciseness, we do not report here the exact bifurcation analysis of the local dynamics.

4 Dynamical indicators

We assess the validity of our model by computing two instantaneous dynamical systems metrics for both ERA-Interim data and the coupled map lattice. Specifically, we consider: the local dimension d of the attractor and the stability θ^{-1} of phase-space trajectories. We briefly outline the physical meaning of these quantities and the way they are computed below.

4.1 Local Dimension

The local dimension is estimated by making use of extreme value statistics applied to recurrences. The Freitas et al. (2010) theorem and its modification by Lucarini et al. (2012) states that the probability of entering a ball of small radius centered on ζ obeys a generalized Pareto distribution (Pickands III, 1975) for chaotic attractors. In order to compute this probability empirically, we first calculate the series of distances $\mathrm{dist}(x(t), \zeta)$ between the point on the attractor ζ and all other points $(x(t))$ on the trajectory. This series is transformed via the distance function:

$$g(x(t)) = -\log(\mathrm{dist}(x(t), \zeta)), \tag{7}$$

such that nearby recurrences to ζ correspond to large values of $g(x(t))$ Collet and Eckmann (2009). Thus, the probability of entering a small ball at ζ is transformed into the probability of exceeding a high threshold q. In the limit of an infinitely long trajectory, it can be shown that the choice $g(x(t))$ in Eq. (7) locks this probability into the exponential member of the generalized Pareto distribution:

$$\Pr(g(x(t)) > q, \zeta) \simeq \exp(-[x - \mu(\zeta)]/\beta(\zeta)), \tag{8}$$

where μ and β (obtained via fitting) depend on the point ζ. Remarkably, $\beta(\zeta) = 1/d(\zeta)$, where $d(\zeta)$ is the local dimension around the point ζ. This result has been recently applied to sea-level pressure fields in Faranda et al. (2017b). In this paper, we use the quantile 0.975 of the series $g(x(t))$ to determine q. We have checked that our results are robust with respect to reasonable changes in this quantile.

4.2 Local Persistence

Extreme value statistics also provides a way of estimating local stability, by inspecting the temporal evolution of the dynamics around ζ. In particular, it is of interest to know the mean residence time of the trajectory within the neighborhood of ζ. To measure this quantity, we employ the so-called extremal index θ (Freitas et al., 2012; Faranda et al., 2016a), which can be thought of as the inverse of this mean residence time. Heuristically, if the ith visit to the neighbourhood of ζ lasts τ_i (i.e. τ_i consecutive time steps), and N such visits are made in total, then $\theta^{-1} \approx (1/N)\sum_i \tau_i$, where $\theta \in [0,1]$. $\theta = 0$ corresponds to a stable fixed point of the dynamics so that the trajectory resides an infinite amount of time in the neighbourhood of ζ. $\theta = 1$ corresponds to residing in the neighbourhood of ζ for only one time step per visit. In practice, the estimate of θ is sensitive to the value of the time step dt used. If dt is too large, the time dependence structure is unresolved and θ will be close to 1. Conversely, if dt is too small, θ is close to zero. In Faranda et al. (2017b) it has been observed for sea-level pressure fields over the North Altantic that θ varies between 0.3 and 0.5, when $dt = 1$ day. In this work we use the same dt. The extremal index is estimated using the likelihood estimator of Süveges (2007).

4.3 Dynamical properties of ERA-Interim jet position data

We illustrate the use of the above metrics on the ERA-Interim jet position data. Figure 5-a) plots the local dimension d versus inverse persistence θ for each day of the data set. The colour scale represents the breaking index BRI. Panels b) and c) show the cross-correlation between BRI and d and θ, respectively. BRI is highly correlated with d. The more breaks in the zonal flow, the higher the local dimension. This result is consistent with the findings of Faranda et al. (2017b) for the North Atlantic region. BRI is also correlated with θ: the more breaks, the lower the persistence of the flow. The shape and range of values of the d–θ diagram are very close to those found for sea-level pressure fields over the Northern Hemisphere (Faranda et al., 2017a). This supports the claim that the position of the jet is indicative of large-scale features of the NH atmospheric circulation. Similar claims about the relevance of low dimensional projections in describing the atmospheric circulation at mid-latitudes are presented by Madonna et al. (2017). In the following, we will use these dynamical properties as guidelines when choosing the best parameters of our model.

5 Results: Comparison of model and reanalysis dynamical properties

We next analyze the bifurcation structure, the spatio-temporal dynamics and the dynamical properties (local dimension, persistence and BRI) of the coupled lattice model defined in Sec. 3. The bifurcation diagram in Figure 6 is constructed by plotting the empirical density of the jet position $\rho(x)$ at fixed longitude (240° W) as a function of ϵ for a) $r = 0$ (spatial homogeneity)

and b) $r^{(i)} = 0.02 (i \in \text{land})$ and $r^{(i)} = -0.04 (i \in \text{ocean})$. The parameter values used are $\eta = 1$, $bl = 15$, $\delta = 10^{-4}$. Three different regimes emerge: i) for small ϵ, CJ fluctuates around a fixed latitude with rare excursions towards NJ and SJ; ii) for large ϵ, the system is pushed from NJ to SJ, and never stabilizes around the CJ; iii) for intermediate ϵ, the jet is centered around its central position CJ on average, but with relatively frequent excursions towards NJ and SJ. We claim, as discussed below,

5   that this is the state that qualitatively resembles the BRI from the reanalysis. The addition of the geographical inhomogeneity (Figure 6 b)) does not change this qualitative picture, but modifies the region of bifurcations and the relative proportions of time spent in SJ versus NJ. Moreover, an asymmetric land/ocean distribution also implies a southward shift of the average CJ position with increasing coupling. This is reminiscent of the behavior in the stochastic bifurcation obtained from the approximated local dynamics (Figure 4).

10   In order to verify the claim that for intermediate ϵ the dynamics of the model matches that of the ERA-Interim data, we analyze other properties of the flow for three different values of ϵ. The results are summarized in Figure 7. The first column of panels (a,e,i,m) display ERA-Interim detrended data, while all other panels display model data with $\epsilon = 0.4$ (b,f,j,n), $\epsilon = 0.01$ (c,g,k,o), $\epsilon = 0.8$ (d,h,l,p). Panels (a-d) display spatial-temporal dynamics for the last 300 days of data or simulations; (e-h) plot auto-correlation functions for the jet position time series at location $240°$ W; (i-l) are snapshots of the jet, where the CJ

15   is displayed in black, NJ in red and SJ in green, and land (model) in magenta; (m-p) plot histograms of the jet position (for all time). From a visual analysis of the spatio-temporal diagrams, we obtain the best qualitative match between model and ERA Interim data for $\epsilon = 0.4$. Over large regions (see the snapshots in panels (i-l)) the transition to SJ and NJ are zonally extensive and progress eastwards. However, we note that the propagation speed in the model is significantly slower than in the ERA-Interim data. This is reflected in the longer tail of the auto-correlation function (compare panels e, f). The distribution of

20   jet positions for $\epsilon = 0.4$ is also qualitatively similar to that of the data (cf. panels m-n), although the latter has a larger positive skewness. It is evident that the output from $\epsilon = 0.01$ (c,g,k,o) and $\epsilon = 0.8$ (d,h,l,p) does not match the qualitative features of the data. When ϵ is small we do not observe SJ and NJ but only small fluctuation around CJ, mostly due to the spatial noise η mimicking the effects of baroclinic waves. When ϵ is large, the system shows very persistent jet deviations.

A more quantitative analysis can be performed by looking at d and θ and their dependence on the BRI for the different

25   simulations discussed above (Figure 8). These can then be compared to the corresponding diagram for the ERA-Interim data (Figure 5), which we show in Figure 8a for ease of comparison. In support of the previous analysis, the dependence of d and θ on BRI for $\epsilon = 0.01$ (Figure 8b) is very close to that obtained for the data, although the dimensions of the model are slightly higher and the persistence lower (i.e. higher θ), and both show a suppressed variance. The simulations with $\epsilon = 0.01$ and $\epsilon = 1$ (Figure 8c, d) again show a larger difference from the reanalysis. For $\epsilon = 0.01$ the persistence is lower (higher θ) and d is

30   constrained to a very narrow range of values, because this state features just one trivial noisy fixed point. In the case $\epsilon = 1$, the persistence is high (θ small) and the range of d is large. Moreover, the BRI index is large because the system experiences very frequent breaks between the SJ and NJ. The few events with low BRI correspond to maxima of d, whereas for the data these events correspond to relatively high values of BRI.

When averaging the instantaneous indicators over all the configurations, regardless of whether they are simulated or ob-

35   served, we obtain the dimension of the attractor D, and the average persistence Θ. For the ERA-Interim data, $D \simeq 13$ and

$\theta \simeq 0.43$. We can therefore scan through the model parameters to find the best fit to the data. The values of D and Θ computed for different model runs are shown in Figure 9. We scan the parameter space by varying the coupling, block length, and noise amplitude. The closest values to those of the reanalysis are obtained with $bl = 20$, $\epsilon = 0.4$, $\eta = 0.6$, $r^{(i)} = 0.01$ ($i \in$ land) and $r^{(i)} = -0.02$ ($i \in$ ocean). This means that, compared to our first guess, the noise amplitude for a realistic representation of the data should be lower. In any case, the spatio-temporal diagram, the snapshot and the distribution for this optimized parameter set looks qualitatively similar to that for $\epsilon = 0.4$ and $\eta = 1$.

6   Conclusions

We have derived a minimal model of the jet stream position dynamics by embedding data extracted from the ERA-Interim reanalysis data set. In comparison to the results obtained for the von Karman flow in Faranda et al. (2017c), the procedure applied here is new and could be adapted to systems with several degrees of freedom. Instead of embedding the data of a global observable in a high-dimensional space, we have constructed the return map for the local position of the jet and then added, via coupling and noise, the physical ingredients recognized in previous studies as drivers of the jet dynamics. The conceptual model is then validated and tuned using local and global dynamical indicators of the data dimension and persistence.

By analyzing the bifurcation structure of the conceptual model as a function of the coupling coefficient — which mimics the coherence of the jet — we identify three behaviors: (i) a strong and uniform jet where large meridional excursions in the jet location are rare extreme events, (ii) a state which is close to the jet dynamics as inferred from the ERA-Interim data, and (iii) a state with sharp meridional excursions, in which the jet is very unstable. Surprisingly, the bifurcation diagram and jet regimes match the possible behaviours obtained from climate change experiments in global climate models, as the solar input (Lachmy and Harnik, 2016) or the obliquity of the Earth (Armstrong et al., 2014; Linsenmeier et al., 2015) are varied.

This study answers some of the questions left open in Faranda et al. (2017a) and Madonna et al. (2017) about the possibility of reducing the complex mid-latitude dynamics to low-dimensional representations given by blocking indices or conceptual models. The fact that the dimension-persistence diagram of the conceptual model qualitatively matches many features of that obtained for the ERA-Interim jet position and the entire sea-level pressure fields of the North Atlantic shows that all the dynamics substantially project along a single line (the jet position). This explains why we observe relatively low dimensions when considering the full sea-level pressure fields. It also suggests that breaks in the jet are responsible for higher dimensions.

This study poses a number of further research questions. The same approach could be applied to the southern hemisphere, where the role of topography is less important. This would allow us to verify some of the hypotheses made here and confirm the influence of topography on the dimension-persistence diagram. Another possibility would be to use the low-dimensional model to build a surrogate data set of the jet positions and then apply this to atmospheric analogues, so as to construct realistic atmospheric dynamics. Finally, it would be interesting to study whether further projections of the atmospheric dynamics to a lower dimensional space are possible, beyond the model developed here, and to test possible relations between different atmospheric blocking indices and the breaking index BRI defined here.

Earth System
Dynamics
Discussions

7   Acknowledgments

Author contributions.   DF and YS performed the analysis and derived the conceptual model. GM computed the jet position data. All the authors participated in the writing and the discussions.

Competing interests.   The authors declare no competing interest.

Earth System
Dynamics
Discussions

References

Archer, C. L. and Caldeira, K.: Historical trends in the jet streams, Geophysical Research Letters, 35, 2008.

Armstrong, J., Barnes, R., Domagal-Goldman, S., Breiner, J., Quinn, T., and Meadows, V.: Effects of extreme obliquity variations on the habitability of exoplanets, Astrobiology, 14, 277–291, 2014.

5 Belmecheri, S., Babst, F., Hudson, A. R., Betancourt, J., and Trouet, V.: Northern Hemisphere jet stream position indices as diagnostic tools for climate and ecosystem dynamics, Earth Interactions, 21, 1–23, 2017.

Collet, P. and Eckmann, J.-P.: Iterated maps on the interval as dynamical systems, Springer Science & Business Media, 2009.

Dee, D. P., Uppala, S., Simmons, A., Berrisford, P., Poli, P., Kobayashi, S., Andrae, U., Balmaseda, M., Balsamo, G., Bauer, d. P., et al.: The ERA-Interim reanalysis: Configuration and performance of the data assimilation system, Quarterly Journal of the royal meteorological

10 society, 137, 553–597, 2011.

Dole, R., Hoerling, M., Perlwitz, J., Eischeid, J., Pegion, P., Zhang, T., Quan, X.-W., Xu, T., and Murray, D.: Was there a basis for anticipating the 2010 Russian heat wave?, Mon Weather Rev, 38, 2011.

Duchon, C. E.: Lanczos filtering in one and two dimensions, Journal of applied meteorology, 18, 1016–1022, 1979.

Faranda, D., Alvarez-Castro, M. C., and Yiou, P.: Return times of hot and cold days via recurrences and extreme value theory, Climate

15 Dynamics, 47, 3803–3815, 2016a.

Faranda, D., Masato, G., Moloney, N., Sato, Y., Daviaud, F., Dubrulle, B., and Yiou, P.: The switching between zonal and blocked mid-latitude atmospheric circulation: a dynamical system perspective, Climate Dynamics, 47, 1587–1599, 2016b.

Faranda, D., Messori, G., Alvarez-Castro, M. C., and Yiou, P.: Dynamical properties and extremes of Northern Hemisphere climate fields over the past 60 years, Nonlinear Processes in Geophysics, 24, 713, 2017a.

20 Faranda, D., Messori, G., and Yiou, P.: Dynamical proxies of North Atlantic predictability and extremes, Scientific reports, 7, 41 278, 2017b.

Faranda, D., Sato, Y., Saint-Michel, B., Wiertel, C., Padilla, V., Dubrulle, B., and Daviaud, F.: Stochastic chaos in a turbulent swirling flow, Physical review letters, 119, 014 502, 2017c.

Frederiksen, J.: A unified three-dimensional instability theory of the onset of blocking and cyclogenesis, J Atmos Sci, 39, 969–982, 1982.

Freitas, A. C. M., Freitas, J. M., and Todd, M.: Hitting time statistics and extreme value theory, Probab Theor Rel, 147, 675–710, 2010.

25 Freitas, A. C. M., Freitas, J. M., and Todd, M.: The extremal index, hitting time statistics and periodicity, Adv Math, 231, 2626–2665, 2012.

Ghil, M.: Dynamics, statistics and predictability of planetary flow regimes, in: Irreversible Phenomena and Dynamical Systems Analysis in Geosciences, pp. 241–283, Springer, 1987.

Hadlock, R. and Kreitzberg, C. W.: The Experiment on Rapidly Intensifying Cyclones over the Atlantic (ERICA) field study: Objectives and plans, Bulletin of the American Meteorological Society, 69, 1309–1320, 1988.

30 Haines, K. and Malanotte-Rizzoli, P.: Isolated anomalies in westerly jet streams: A unified approach, Journal of the atmospheric sciences, 48, 510–526, 1991.

Hansen, A. R.: Observational characteristics of atmospheric planetary waves with bimodal amplitude distributions, Adv Geophys, 29, 101–133, 1986.

Jacoby, T., Read, P., Williams, P. D., and Young, R.: Generation of inertia–gravity waves in the rotating thermal annulus by a localised

35 boundary layer instability, Geophysical & Astrophysical Fluid Dynamics, 105, 161–181, 2011.

Kaneko, K.: Transition from Torus to Chaos Accompanied by Frequency Lockings with Symmetry Breaking: In Connection with the Coupled-Logistic Map, Progress of Theoretical Physics, 69, 1427–1442, 1983.

Kaneko, K.: Spatial period-doubling in open flow, Physics Letters A, 111, 321–325, 1985.

Koch, P., Wernli, H., and Davies, H. C.: An event-based jet-stream climatology and typology, International Journal of Climatology, 26, 283–301, 2006.

Lachmy, O. and Harnik, N.: Wave and Jet Maintenance in Different Flow Regimes, Journal of the Atmospheric Sciences, 73, 2465–2484, 2016.

Lee, S. and Kim, H.-k.: The dynamical relationship between subtropical and eddy-driven jets, Journal of the Atmospheric Sciences, 60, 1490–1503, 2003.

Legras, B. and Ghil, M.: Persistent anomalies, blocking and variations in atmospheric predictability, J Atmos Sci, 42, 433–471, 1985.

Linsenmeier, M., Pascale, S., and Lucarini, V.: Climate of Earth-like planets with high obliquity and eccentric orbits: implications for habitability conditions, Planetary and Space Science, 105, 43–59, 2015.

Lucarini, V., Faranda, D., Turchetti, G., and Vaienti, S.: Extreme value theory for singular measures, Chaos, 22, 023 135, 2012.

Madonna, E., Li, C., Grams, C. M., and Woollings, T.: The link between eddy-driven jet variability and weather regimes in the North Atlantic-European sector, Quarterly Journal of the Royal Meteorological Society, 143, 2960–2972, 2017.

McWilliams, J. C., Flierl, G. R., Larichev, V. D., and Reznik, G. M.: Numerical studies of barotropic modons, Dynam Atmos Oceans, 5, 219–238, 1981.

Mo, K. and Ghil, M.: Cluster analysis of multiple planetary flow regimes, J Geophys Res-Atmos, 93, 10 927–10 952, 1988.

Pickands III, J.: Statistical inference using extreme order statistics, the Annals of Statistics, pp. 119–131, 1975.

Reiter, E. R. and Nania, A.: Jet-stream structure and clear-air turbulence (CAT), Journal of Applied Meteorology, 3, 247–260, 1964.

Röthlisberger, M., Pfahl, S., and Martius, O.: Regional-scale jet waviness modulates the occurrence of midlatitude weather extremes, Geophysical Research Letters, 43, 2016.

Sato, Y., Doan, T., Rasmussen, M., and Lamb, J. S.: Stochastic bifurcation in random logistic maps, arxiv/xxx.xxxxx.

Screen, J. A. and Simmonds, I.: Amplified mid-latitude planetary waves favour particular regional weather extremes, Nature Climate Change, 4, 704, 2014.

Simmons, A., Wallace, J., and Branstator, G.: Barotropic wave propagation and instability, and atmospheric teleconnection patterns, J Atmos Sci, 40, 1363–1392, 1983.

Süveges, M.: Likelihood estimation of the extremal index, Extremes, 10, 41–55, 2007.

Tibaldi, S., Buzzi, A., and Malguzzi, P.: Orographically induced cyclogenesis: Analysis of numerical experiments, Monthly Weather Review, 108, 1302–1314, 1980.

Tung, K. and Lindzen, R.: A theory of stationary long waves. I-A simple theory of blocking. II-Resonant Rossby waves in the presence of realistic vertical shears, 1979.

Weeks, E. R., Crocker, J. C., Levitt, A. C., Schofield, A., and Weitz, D. A.: Three-dimensional direct imaging of structural relaxation near the colloidal glass transition, Science, 287, 627–631, 2000.

Williams, P. D. and Joshi, M. M.: Intensification of winter transatlantic aviation turbulence in response to climate change, Nature Climate Change, 3, 644, 2013.

Williams, P. D., Read, P., and Haine, T.: Spontaneous generation and impact of inertia-gravity waves in a stratified, two-layer shear flow, Geophysical research letters, 30, 2003.

Williams, P. D., Haine, T. W., and Read, P. L.: On the generation mechanisms of short-scale unbalanced modes in rotating two-layer flows with vertical shear, Journal of Fluid Mechanics, 528, 1–22, 2005.

Earth System
Dynamics
Discussions

Woollings, T., Hannachi, A., and Hoskins, B.: Variability of the North Atlantic eddy-driven jet stream, Quarterly Journal of the Royal
   Meteorological Society, 136, 856–868, 2010.
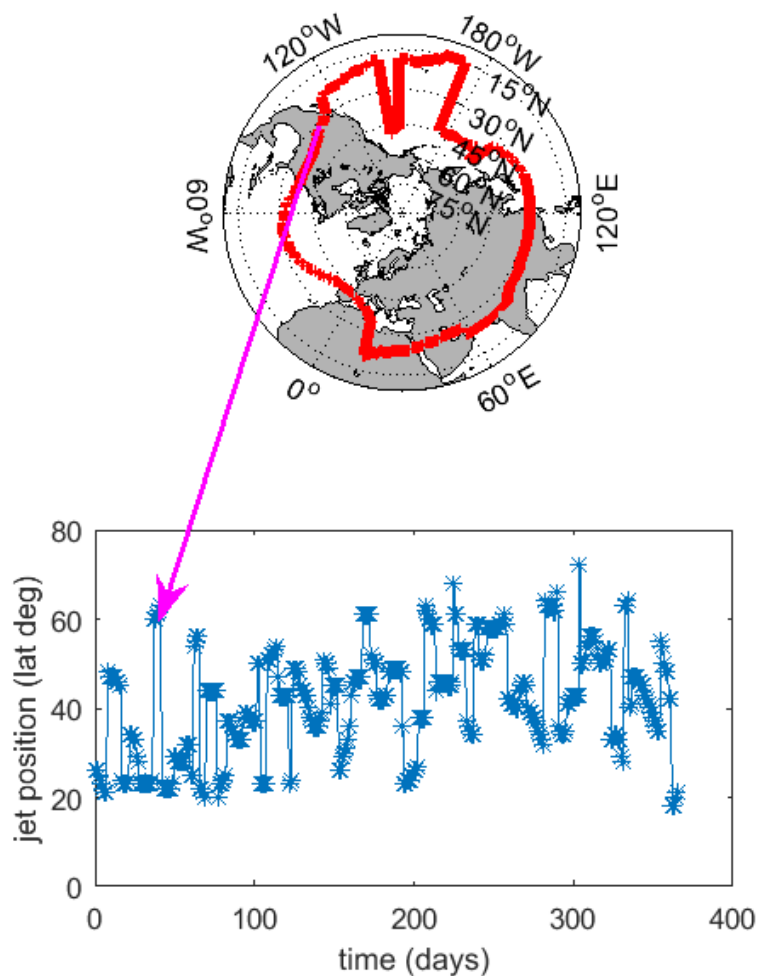
Figure 1. Snapshot of the jet position extracted from the ERA-Interim dataset on Feb 4th 1979 and time series of the jet position for the year 1979, recorded at longitude 120° W.
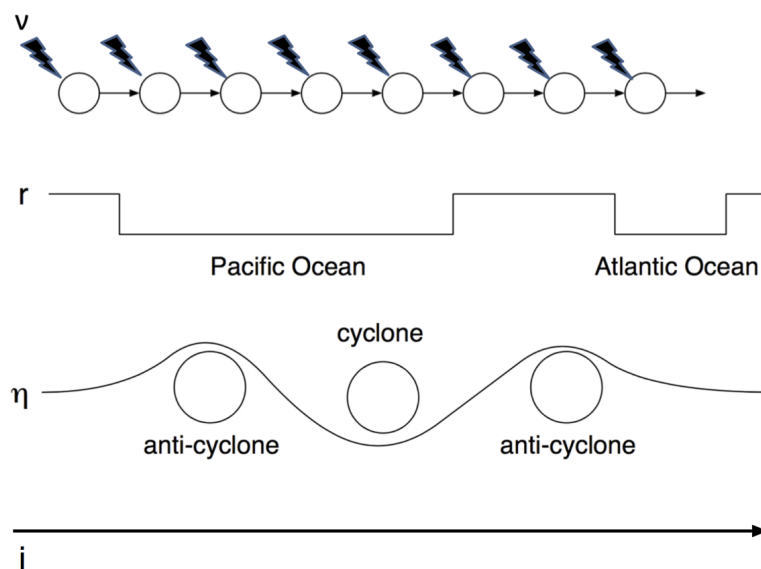
Figure 2. Schematic representation of noise contributions to the CML model (Eq.5): ν represents local turbulent disturbances, r geographical features, η baroclinic eddies, and i spatial positions.

Earth System
Dynamics

Discussions

Open Access

EGU
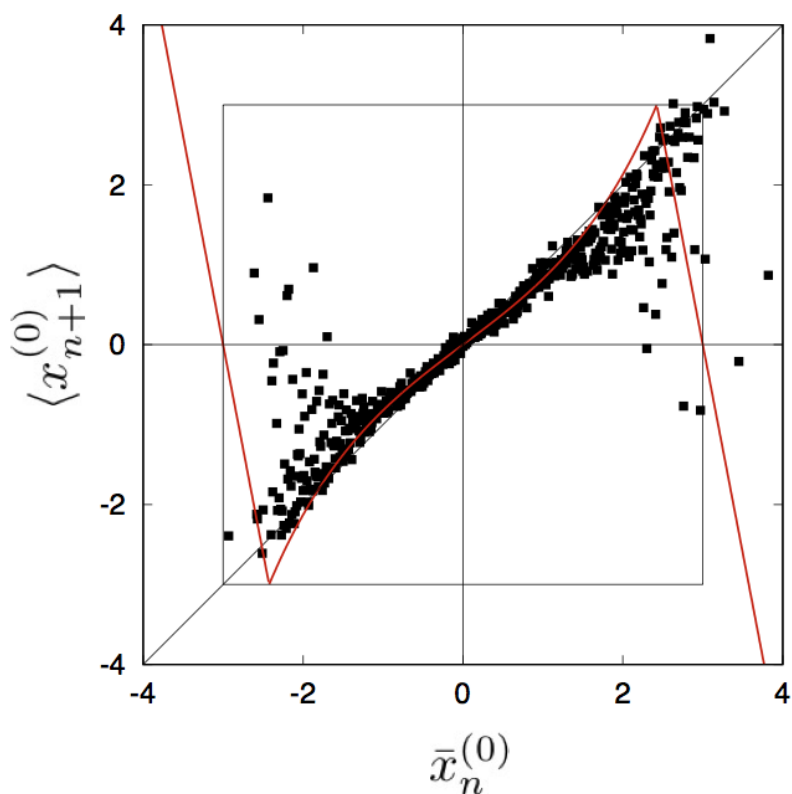
Figure 3. The average return map extracted from the data at longitude $i = 0$. The black dots are the observed data $\langle x_{n+1} \rangle$ averaged over each median $\bar{x}_n$. The red line represents the approximated averaged return map (Eq. 4).

Earth System
Dynamics
Discussions
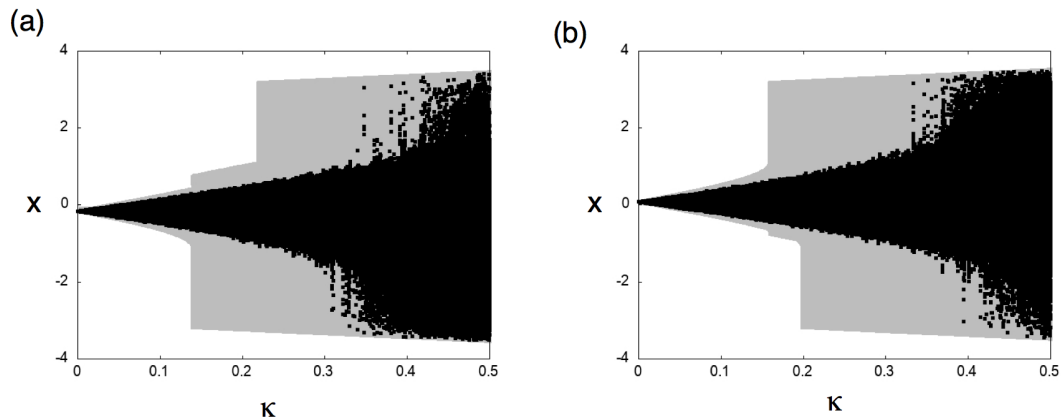
Figure 4. Bifurcation diagrams as a function of κ for (a) land ($r^{(i)} = -0.04$) and (b) ocean ($r^{(i)} = 0.02$). The grey regions are minimal invariant sets, which delimit the accessible region of the dynamics with respect to all possible external perturbations. A realization of the dynamics with $\{p_n^{(i)}\}$ is given by the black dots. For $r^{(i)} = -0.04$ ($r^{(i)} = 0.02$) and $0.136\ldots < \kappa < 0.217\ldots$ ($0.156\ldots < \kappa < 0.196\ldots$), there is a small chance to reach SJ (NJ) positions and no chance to reach NJ (SJ) positions.
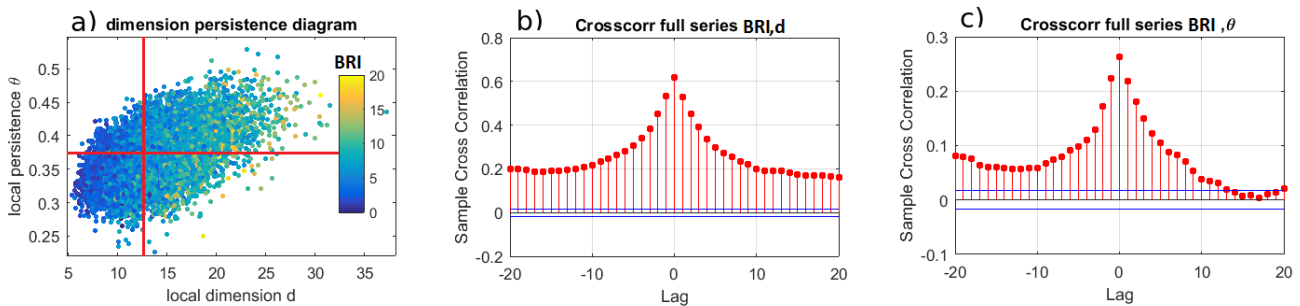
Figure 5. a) Dimension-persistence diagram for the ERA-Interim jet data from 1979-2016. Each point represents the local dimension d and inverse persistence θ for a given day in the data set. The colour scale indicates the number of breaks measured by the BRI. b) Cross-correlation between BRI and local dimension d. c) Cross-correlation between BRI and inverse persistence θ.

Earth System
Dynamics

Discussions

Open Access
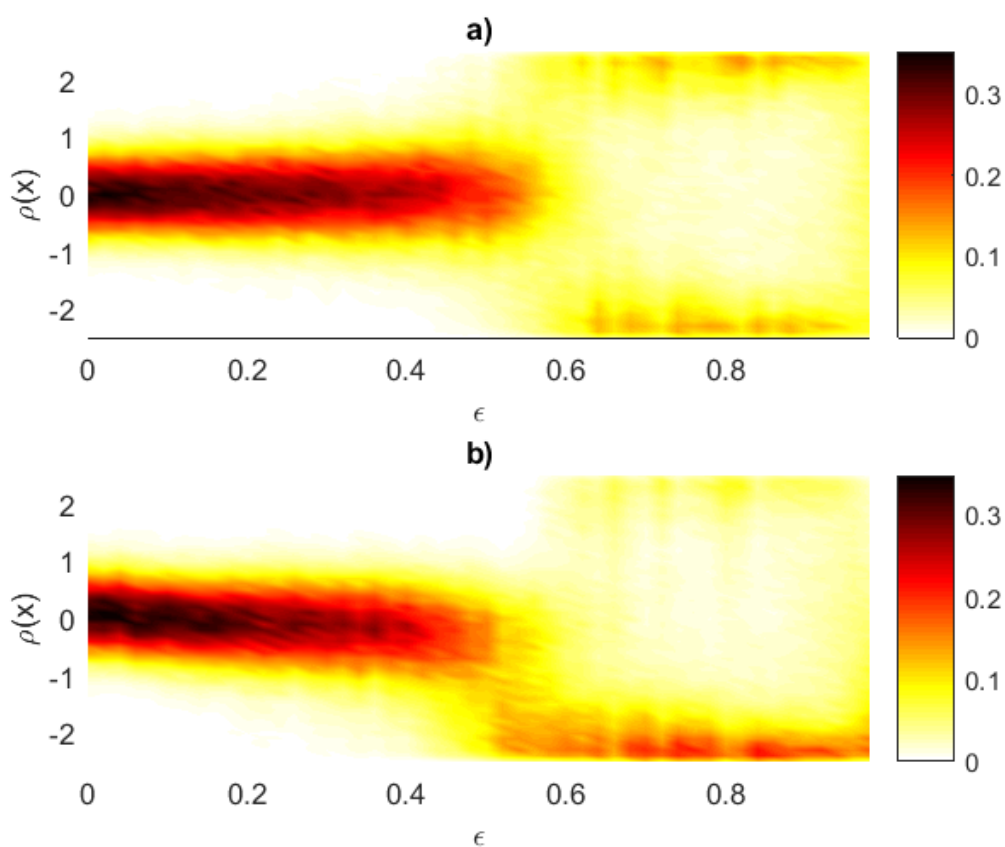
Figure 6. Bifurcation diagram in terms of the density $\rho(x)$, at longitude $120°$ W, as a function of ϵ. a) $r = 0$ (no spatial inhomogeneity), b) $r^{(i)} = 0.02$ ($i \in$ land) and $r^{(i)} = -0.04$ ($i \in$ ocean). The parameter values are $\eta = 1$, $bl = 15$ and $\delta = 10^{-4}$.
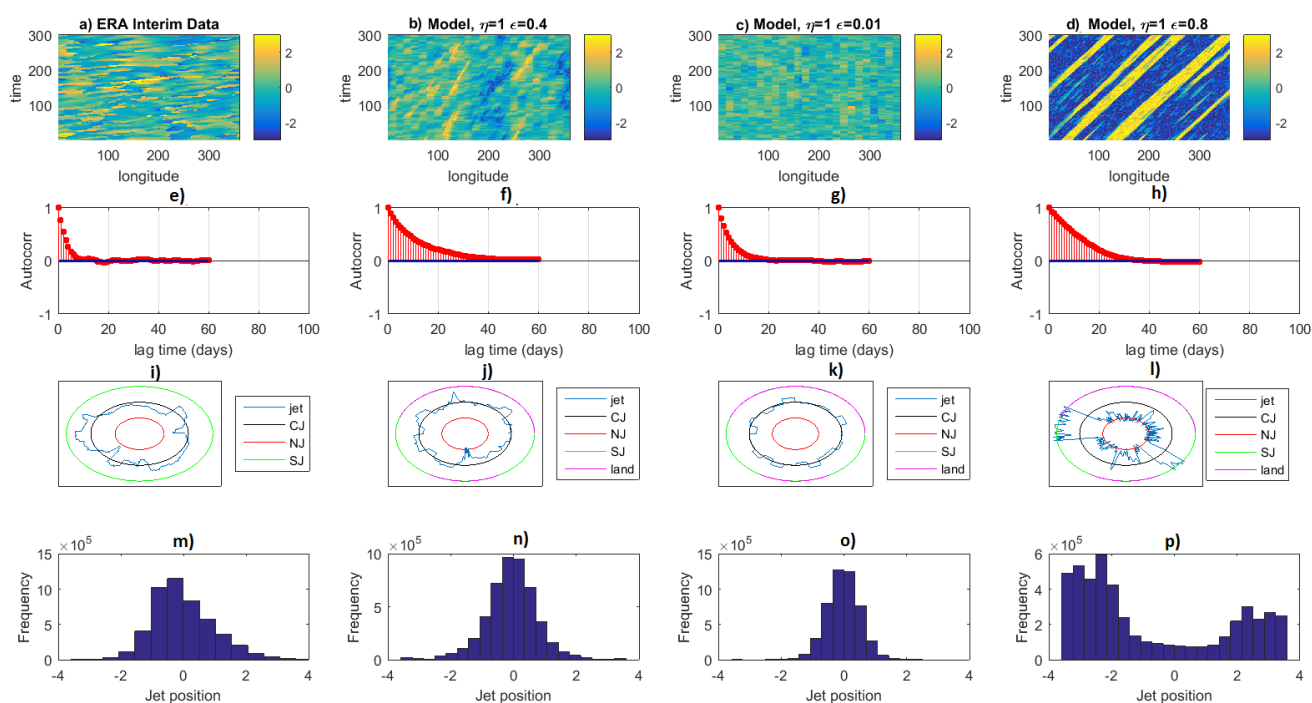
Figure 7. Comparison between ERA-Interim data and model for different parameter sets: (a-d) spatial-temporal diagrams for the last 300 days of data; (e-h) auto-correlation functions for the jet position time series at location $120°$ W; (i-l) snapshots of the jet, with CJ in black, NJ in red, SJ in green and land position (model) in magenta; (m-p) histograms of the jet position at all latitudes and times. Plots (a,e,i,m) refer to the ERA-Interim detrended data; other plots refer to the model with $\eta = 1$, $bl = 15$, $\delta = 10^{-4}$, and $\epsilon = 0.4$ (b,f,j,n), $\epsilon = 0.01$ (c,g,k,o), $\epsilon = 0.8$ (d,h,l,p).
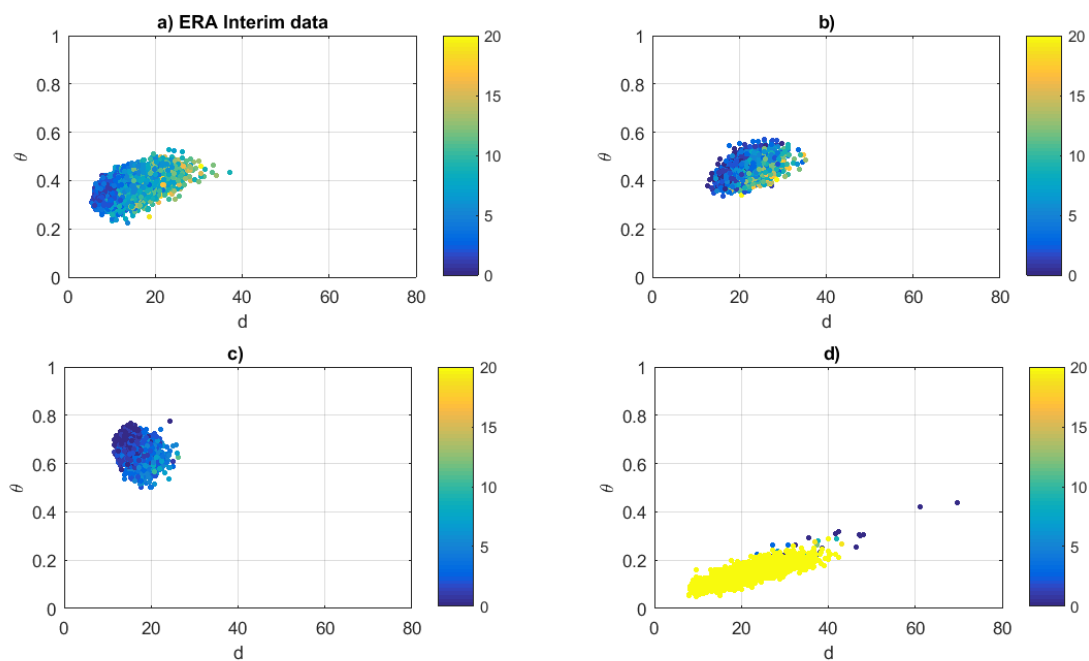
Figure 8. Dimension-persistence diagrams for a) ERA-Interim data (same as Figure 5-a)). (b-d) the three model simulations shown in Figure 7 with b), $\epsilon = 0.4$; (c), $\epsilon = 0.01$, (d), $\epsilon = 0.8$. Each point represents the value of the local dimension d and inverse persistence θ for a given day in the dataset. The colour scale indicates the number of breaks measured by the BRI.

Earth System
Dynamics
Discussions

Open Access
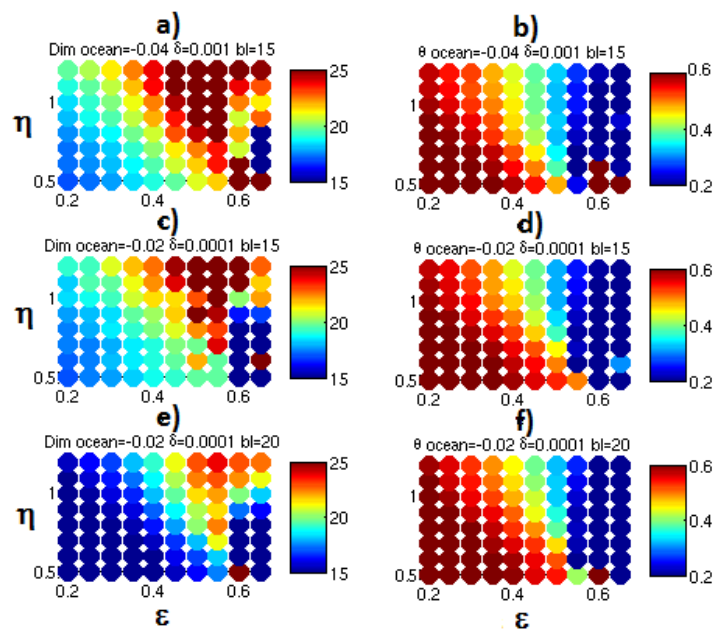
Figure 9. Attractor dimension D (a,c,e) and average persistence Θ (b,d,f) for different parameters of the model. a,b) $\delta = 10^{-3}$, $r^{(i)} = 0.02(i \in \text{land})$ and $r^{(i)} = -0.04(i \in \text{ocean})$, $bl = 15$. c,d) $\delta = 10^{-4}$, $r^{(i)} = 0.01(i \in \text{land})$ and $r^{(i)} = -0.02(i \in \text{ocean})$, $bl = 15$. e,f) $\delta = 10^{-4}$, $r^{(i)} = 0.01(i \in \text{land})$ and $r^{(i)} = -0.02(i \in \text{ocean})$, $bl = 20$.